

Utilization of Coupling Effects in Compensator Design for Structural Acoustic Systems *

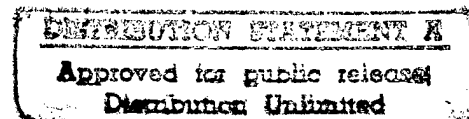
H.T. Banks and M.A. Demetriou
Center for Research in Scientific Computation
North Carolina State University
Raleigh, NC 27695-8205

R.C. Smith
Department of Mathematics
Iowa State University
Ames, IA 50011

Abstract

The quantification and utilization of coupling effects in a prototypical structural acoustic system are examined in this paper. In typical systems, the coupling mechanisms are manifested in two ways. The first leads to the transfer of energy from an ambient field to an adjacent structure and is often responsible for exogenous structural excitation. The second involves the transfer of energy from the vibrating structure to an adjacent field. This is the source of structure-borne noise and is ultimately the mechanism through which structural actuators are utilized to attenuate noise. The examples presented here demonstrate that in fully coupled systems, both mechanisms should be incorporated to accurately model system dynamics. The examples also illustrate advantages and limitations of compensators which utilize the accurate modeling of the structural coupling.

19961121 110



*Research supported in part (H.T.B. and M.A.D.) by the Air Force Office of Scientific Research under grant AFOSR F49620-95-1-0236, and in part (M.A.D. and R.C.S.) by NASA under grant NAG-1-1600. Research was also supported by NASA under Contract Number NAS1-19480 while H.T.B. and R.C.S. were visiting scientists at ICASE, NASA Langley Research Center.

1 Introduction

The control of noise and vibration in structural acoustic systems has been intensely investigated in applications ranging from aircraft design to transformer construction. The trademark of all such applications and the mechanism ultimately utilized for control is the inherent coupling between the structure and adjacent acoustic fields. This mechanism is manifested in two ways. In the first, energy from a vibrant field is transmitted to a structure through pressure or force coupling. This is the mechanism responsible for fuselage vibrations due to propeller draft or vibrations in the casing surrounding a transformer. Unattenuated vibration due to the acoustic or fluid/structure coupling can lead to structural fatigue. It can also lead to the second mechanism of coupling in which energy is transmitted from the structure to an acoustic or compressible fluid field. This is the source of structure-borne noise and is ultimately the mechanism through which structural actuators are used to attenuate noise.

Accurate modeling of the acoustic, structural and coupling components is a necessary first step for predicting the dynamics of structural acoustic systems and the design of model-based controllers. Substantial effort has been directed toward structural systems, and adequate linear models for various geometries have been developed. Moreover, as illustrated in [9], model-based controllers employing piezoceramic actuators have been experimentally implemented. The case for large displacements and hence nonlinear structural models is less complete.

Similarly, linear wave models have been successfully utilized for low sound pressure level acoustic applications. Like the structural case, appropriate nonlinear models for large sound pressure levels are still under investigation. An important issue when modeling the acoustic field concerns the relatively low wave speeds at general atmospheric conditions. This leads to delays between the input of a signal to a structure-mounted actuator and measurement of the corresponding response at an acoustic sensor. If left unmodeled or uncompensated, this delay can destabilize a controller. This motivates the use of a dynamic wave model which incorporates the physical transmission time.

The analysis of coupling mechanisms is less complete than that of the other components. In the structural acoustic systems described in [5, 6, 10] and references therein, pressure coupling provided the mechanism for energy transfer from the field to the structure while velocity coupling yielded the converse effect. Modal coupling, radiation efficiency and radiation impedance were employed in [12, 13, 18] where the problem of attenuating structure-borne noise was considered. These coupling techniques are concerned with describing the transfer of energy from the structure to the field to address the objective of reducing the efficiency of structural radiation. The coupling between a nonlinear acoustic/fluid field and a structure through pressure balancing was employed in [15, 17] while pressure balancing was again used in [16] for modeling the converse effect of acoustic radiation from a vibrating panel. In these latter investigations, partial differential equations (PDE) derived from physical principles such as force and momentum balancing were used to model the fluid/acoustic/structural dynamics; however, these coupled models have not yet been utilized in acoustic control laws.

In this work, we quantify and utilize the two coupling effects for compensator design in a prototypical 3-D structural acoustic system. This significantly extends the results of [5, 10] due to the higher dimensional complexity and analysis pertaining to compensator improvements through utilization of the coupling. It differs from [12, 13, 18] in that coupled PDE are used to model the system and provide a basis for the control laws. Modeling the system in this manner

helps to provide insight for simulations and the development of model-based controllers.

The advantage of accurate quantification of the coupling mechanisms for the purpose of modeling system dynamics is obvious. The potential advantages from the perspective of control design can be indicated through a brief overview of various aspects concerning a feedback controller utilizing structural actuators.

In the idealized case of full state feedback control, information regarding the discretized structural acoustic model and control operator is used to compute a Riccati solution and corresponding gain. This gain is then applied to the state to compute a control signal which is fed back to the structural actuators. Control of the structure-borne noise is realized due to the natural "feedback loop" which results from the structural acoustic coupling. In this case, the model provides the system information necessary for attaining an accurate Riccati solution and hence gain. Note that this case is idealized in the sense that it requires knowledge of the full structural (displacement, velocity) and acoustic (potential, pressure) states which is not possible with current instrumentation.

A more realistic scenario when implementing the controller is one in which a limited number of structural and/or acoustic measurements are available. In this case, the model is first used to provide system information for an observer Riccati equation necessary for estimating or reconstructing the state. The data for these calculations consists in part of the structural and/or acoustic measurements. The feedback gain is then applied to the state estimate to obtain the control signal. The model plays a dual role in this case since it provides system information used in calculating both the state estimate and the feedback gain.

The second source of system information is the data collected from structural and/or acoustic sensors. In applications involving an enclosed or interior field (e.g., an aircraft cabin), it may be possible to use both structural (e.g., accelerometers or piezoceramic patches) and acoustic (e.g., microphones) sensors. To reduce weight and hardware requirements, however, it is often advantageous to limit the number of sensors. This places the impetus for accurate system predictions on the model. In other applications such as reduction of exterior noise generated by a transformer or an underwater vehicle, it is difficult, and in many cases impossible, to employ acoustic sensors. In such cases, the acoustic state and feedback gain must be calculated solely using the coupled model with structural data as input. For both interior and exterior noise control applications, the success of the controller is contingent upon the accuracy of the acoustic, coupling and structural components of the model.

We consider here various aspects concerning the utilization of coupling in a 3-D structural acoustic system. In Section 2, we present the model and outline the general feedback control methodology for the system. Numerical simulations demonstrating the effects of the two coupling mechanisms are presented in Section 3. It is demonstrated that for systems subjected to the two effects, both coupling mechanisms must be incorporated in the model to attain the correct system dynamics and frequencies. Control simulations for a system having the geometry and dimensions of an experimental device used in the Acoustics Division, NASA Langley Research Center, are presented in Section 4. These results demonstrate that even with a limited number of structural and acoustic sensors, significant attenuation is attained with the model-based controllers. The dimensions of the acoustic cavity relative to the vibrating surface are significantly increased in Section 5. This illustrates certain controllability issues which must be addressed when employing structure-mounted actuators to control large acoustic fields. Section 6 contains a summary of numerical results demonstrating the design of a

purely structural controller. These results show that such a controller provides adequate attenuation for exogenous frequencies near *isolated* structural frequencies, but has minimal effect when acoustic-like modes are excited. Taken in concert, these examples demonstrate advantages and limitations of controllers which utilize accurate modeling of the structural acoustic system.

From these results, the main contributions of this paper can be summarized as follows. With regard to modeling, the numerical simulations demonstrate the manner through which natural frequencies for the fully coupled system are modified from those of the isolated structural and acoustic components. The coupling between components also leads to corresponding modal changes. From a control perspective, the numerical examples demonstrate that for this geometry, little control authority is lost by employing a realizable output feedback compensator as compared with an impractical full state LQR theory. It is further demonstrated that for this system, very adequate attenuation can be obtained via a compensator which incorporates the fully coupled model but utilizes only structural sensors. While the degree of attenuation achieved in this manner is application dependent, these results illustrate the potential for reduced hardware through accurate modeling. Finally, the results illustrate that the reduction of structural vibrations via isolated structural models is not adequate for controlling broadband structure-borne noise. The acoustic field and coupling mechanisms must also be incorporated in the model to attain effective noise reduction.

2 Model and Control Formulation

The first step in the development of a model-based control methodology is the derivation of a system model. This is illustrated here for a structural acoustic test apparatus used in the Acoustics Division, NASA Langley Research Center. This apparatus consists of a concrete cylinder with a thin aluminum plate mounted at one end as depicted in Figure 1. The opposite end is closed so that interior acoustic waves are reflected back toward the plate. A loudspeaker adjacent to the plate provides an exterior acoustic source while surface-mounted piezoceramic patches are used as control elements. Note that in this system, both coupling between the plate and interior field and pressure interactions between the interior/exterior acoustic field and plate are present.

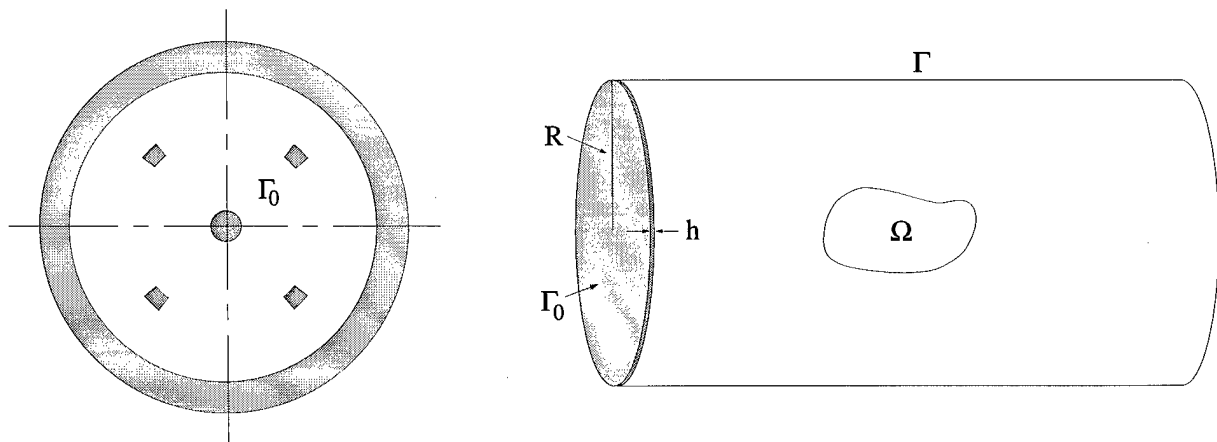


Figure 1. Cylindrical structural acoustic system with a fixed plate at one end.

To specify the geometry, the cylinder is assumed to have length ℓ and radius R with a thin plate of thickness h at one end. The interior acoustic domain is denoted by Ω while Γ_0 indicates the plate domain. The remaining boundary of the acoustic cavity is denoted by Γ and has an outward normal \hat{n} .

The test apparatus just described is a hybrid system in several senses. The generation of interior noise is due to structural acoustic coupling while control via the piezoceramic patches is due to electromechanical interactions. Finally, the system contains several electromagnetic components due to the hardware required for sensing and control. We describe here PDE modeling the structural, acoustic and structural acoustic coupling components as well as the electromechanical input from the patches. When spatially discretized, this provides a vector ODE which approximates the dynamics of the acoustic and mechanical components of the experimental system. Various uncertainties are then incorporated in the model to account for model and sensing uncertainties as well as the unmodeled electromagnetic components. The section concludes with an H^∞ /MinMax formulation appropriate for the ODE system with uncertainties.

2.1 System Model

Interior Acoustic Field

For the purpose of modeling the interior acoustic field dynamics, it is assumed that sound pressure levels are below 120 dB and that acoustic field damping is negligible. These are reasonable and typical assumptions when considering the sound pressure levels and dimensions of the experimental device or in applications such as control of fuselage noise. Furthermore, it is assumed that the acoustic cylinder and endcap are not influenced by the interior acoustic field; that is, no concrete pipe or endcap frequencies are found in the system response. This latter assumption has been verified through accelerometer tests with the experimental apparatus.

With ϕ and c denoting an acoustic velocity potential and wave speed, respectively, an appropriate model for the interior acoustic dynamics is

$$\begin{aligned} \frac{\partial^2 \phi}{\partial t^2} &= c^2 \Delta \phi & , \quad (r, \theta, z) \in \Omega, t > 0, \\ \nabla \phi \cdot \hat{n} &= 0 & , \quad (r, \theta, z) \in \Gamma, t > 0 \end{aligned} \tag{2.1}$$

with the Laplacian in cylindrical coordinates given by

$$\Delta \phi = \frac{\partial^2 \phi}{\partial r^2} + \frac{1}{r} \frac{\partial \phi}{\partial r} + \frac{1}{r^2} \frac{\partial^2 \phi}{\partial \theta^2} + \frac{\partial^2 \phi}{\partial z^2}.$$

The linear wave equation provides an adequate approximation of the acoustic dynamics for the sound pressure levels under consideration. This includes the dynamic effects which account for the time required to propagate information from the plate to sensors in the cavity. The hardwall boundary conditions are justified by the inert nature of the concrete cylinder and endcap with the form of the boundary conditions resulting from the inherent relationship between the acoustic potential and velocity (i.e., $v = -\nabla \phi$). Finally, we note that the

potential is related to the acoustic pressure through the relationship $p = \rho_f \frac{\partial \phi}{\partial t}$ where ρ_f denotes the equilibrium density of the interior acoustic field.

Plate Dynamics

In developing dynamic equations for the plate, it is assumed that the displacements are within the range of linear theory and that rotational effects are negligible. Both of these assumptions have been validated through parameter estimation for the plate in the experimental setup (see [8]). Furthermore, it is assumed that s piezoceramic patch pairs are bonded to the plate and driven out-of-phase so as to produce pure bending moments. Finally, it is assumed that boundary clamps are sufficiently tight to permit the use of clamped-edge boundary conditions. This latter assumption is again justified by the experimental results in [8].

As detailed in [7, 22], an appropriate model for the circular plate derived under the assumption of negligible air damping is

$$\rho h \frac{\partial^2 w}{\partial t^2} - \frac{\partial^2 \mathcal{M}_r}{\partial r^2} - \frac{2}{r} \frac{\partial \mathcal{M}_r}{\partial r} + \frac{1}{r} \frac{\partial \mathcal{M}_\theta}{\partial r} - \frac{2}{r} \frac{\partial^2 \mathcal{M}_{r\theta}}{\partial r \partial \theta} - \frac{2}{r^2} \frac{\partial \mathcal{M}_{r\theta}}{\partial \theta} - \frac{1}{r^2} \frac{\partial^2 \mathcal{M}_\theta}{\partial \theta^2} = g(t, r, \theta),$$

$$w(t, R, \theta) = \frac{\partial w}{\partial r}(t, R, \theta) = 0$$

where w is the transverse plate displacement, ρ is the structural density and g is a general surface force input term. The general moments are given by

$$\begin{aligned}\mathcal{M}_r &= M_r - (M_r)_{pe} \\ \mathcal{M}_\theta &= M_\theta - (M_\theta)_{pe} \\ \mathcal{M}_{r\theta} &= M_{r\theta}\end{aligned}$$

where M_r, M_θ and $M_{r\theta}$ are internal plate moments and $(M_r)_{pe}$ and $(M_\theta)_{pe}$ are the external moments generated by the patches.

The internal moments for the circular plate with s pairs of surface-mounted piezoceramic patches have the form

$$\begin{aligned}M_r &= DK_r + \tilde{D}K_\theta + c_D \dot{K}_r + \tilde{c}_D \dot{K}_\theta \\ M_\theta &= DK_\theta + \tilde{D}K_r + c_D \dot{K}_\theta + \tilde{c}_D \dot{K}_r \\ M_{r\theta} &= M_{\theta r} = \frac{D}{2} \tau - \frac{\tilde{D}}{2} \tau + \frac{c_D}{2} \dot{\tau} - \frac{\tilde{c}_D}{2} \dot{\tau}\end{aligned}\tag{2.2}$$

where

$$K_r = -\frac{\partial^2 w}{\partial r^2}, \quad K_\theta = -\frac{1}{r} \frac{\partial w}{\partial r} - \frac{1}{r^2} \frac{\partial^2 w}{\partial \theta^2}, \quad \tau = -\frac{2}{r} \frac{\partial^2 w}{\partial r \partial \theta} + \frac{2}{r^2} \frac{\partial w}{\partial \theta}.$$

The global flexural rigidity parameters D, \tilde{D} and Kelvin-Voigt damping parameters c_D and

\tilde{c}_D are given by

$$\begin{aligned}
D(r, \theta) &= \frac{E_p h^3}{12(1 - \nu_p^2)} + \frac{2}{3} \sum_{i=1}^s \left[\frac{E_{pe} a_{3pe}}{1 - \nu_{pe}^2} + \frac{E_{b\ell} a_{3b\ell}}{1 - \nu_{b\ell}^2} \right] \chi_i(r, \theta) \\
\tilde{D}(r, \theta) &= \frac{E_p h^3 \nu_p}{12(1 - \nu_p^2)} + \frac{2}{3} \sum_{i=1}^s \left[\frac{E_{pe} a_{3pe} \nu_{pe}}{1 - \nu_{pe}^2} + \frac{E_{b\ell} a_{3b\ell} \nu_{b\ell}}{1 - \nu_{b\ell}^2} \right] \chi_i(r, \theta) \\
c_D(r, \theta) &= \frac{\hat{c}_{D_p} h^3}{12(1 - \nu_p^2)} + \frac{2}{3} \sum_{i=1}^s \left[\frac{\hat{c}_{D_{pe}} a_{3pe}}{1 - \nu_{pe}^2} + \frac{\hat{c}_{D_{b\ell}} a_{3b\ell}}{1 - \nu_{b\ell}^2} \right] \chi_i(r, \theta) \\
\tilde{c}_D(r, \theta) &= \frac{\hat{c}_{D_p} h^3 \nu_p}{12(1 - \nu_p^2)} + \frac{2}{3} \sum_{i=1}^s \left[\frac{\hat{c}_{D_{pe}} a_{3pe} \nu_{pe}}{1 - \nu_{pe}^2} + \frac{\hat{c}_{D_{b\ell}} a_{3b\ell} \nu_{b\ell}}{1 - \nu_{b\ell}^2} \right] \chi_i(r, \theta)
\end{aligned} \tag{2.3}$$

where the Young's modulus, density coefficient, Poisson ratio and Kelvin-Voigt damping coefficient for the plate are denoted by E_p, ρ_p, ν_p and \hat{c}_{D_p} , respectively, while similar parameters for the patches and bonding layer are denoted by $E_{pe}, \rho_{pe}, \nu_{pe}, \hat{c}_{D_{pe}}$ and $E_{b\ell}, \rho_{b\ell}, \nu_{b\ell}, \hat{c}_{D_{b\ell}}$, respectively. The constants $a_{3b\ell} \equiv (h/2 + T_{b\ell})^3 - (h/2)^3$, $a_{3pe} \equiv (h/2 + T_{b\ell} + T)^3 - (h/2 + T_{b\ell})^3$ arise from integration through the bonding layer $T_{b\ell}$ and patch thickness T while $\chi_i(r, \theta)$ denotes the characteristic function which has a value of 1 in the region covered by the i^{th} patch and is 0 elsewhere. Finally, the mass density also exhibits a piecewise constant nature due to the presence of the patches and is given by

$$\rho(r, \theta) = \rho_p + \frac{2}{h} \sum_{i=1}^s [\rho_{b\ell} T_{b\ell} + \rho_{pe} T] \chi_i(r, \theta).$$

We point out that if the plate, patches and bonding layers have the same Poisson ratios ($\nu_p = \nu_{pe} = \nu_{b\ell} = \nu$), then the internal moment expressions reduce to the familiar relations for a thin plate with variable thickness due to the bonding layers and patches. For example, M_r in this case is given by

$$M_r = -D \left(\frac{\partial^2 w}{\partial r^2} + \frac{\nu}{r} \frac{\partial w}{\partial r} + \frac{\nu}{r^2} \frac{\partial^2 w}{\partial \theta^2} \right) - c_D \left(\frac{\partial^3 w}{\partial r^2 \partial t} + \frac{\nu}{r} \frac{\partial^2 w}{\partial r \partial t} + \frac{\nu}{r^2} \frac{\partial^3 w}{\partial \theta^2 \partial t} \right)$$

with D and c_D defined in (2.3).

The external moments generated by the patches in response to an applied voltage (out-of-phase for the patch pair) are given by

$$(M_r)_{pe} = (M_\theta)_{pe} = - \sum_{i=1}^s \mathcal{K}_i^B u_i(t) \chi_i(r, \theta) \tag{2.4}$$

where $u_i(t)$ is the voltage into the i^{th} patch pair and \mathcal{K}_i^B is a parameter which depends on the geometry, piezoceramic and plate material properties, and piezoelectric strain constant (see [11] for details). Note that (2.4) accounts for the electromechanical coupling through which an applied voltage is converted to mechanical input.

Structural Acoustic Coupling

Two structural acoustic coupling mechanisms are inherent in the system. The first accounts for the influence of the internal and external acoustic fields on the structure. It yields the input term

$$g(t, r, \theta) = f(t, r, \theta) - \rho_f \frac{\partial \phi}{\partial t}(t, r, \theta, w(t, r, \theta))$$

where f is a surface force modeling the exogenous loudspeaker input and $\rho_f \frac{\partial \phi}{\partial t} = p$ is the backpressure force due to the interior field. The second mechanism is responsible for the transfer of energy from the plate to the interior field. It is modeled by the continuity of velocity condition

$$\frac{\partial \phi}{\partial z}(t, r, \theta, w(t, r, \theta)) = -\frac{\partial w}{\partial t}(t, r, \theta) \quad , \quad (r, \theta) \in \Gamma_0, \quad t > 0$$

(recall that due to the definition of the potential ϕ , $\frac{\partial \phi}{\partial z}$ is the acoustic velocity in the z -direction). Because both conditions occur at the moving plate surface, they are inherently nonlinear. Under the assumptions of small displacements, however, it is reasonable to linearize about the rest state to obtain

$$g(t, r, \theta) = f(t, r, \theta) - \rho_f \frac{\partial \phi}{\partial t}(t, r, \theta, 0)$$

$$\frac{\partial \phi}{\partial z}(t, r, \theta, 0) = -\frac{\partial w}{\partial t}(t, r, \theta)$$

(see [6] for numerical investigations validating this assumption).

Strong Form of System Model

Consolidation of components yields the strong form of the coupled acoustic/structural/electromechanical model

$$\begin{aligned} \frac{\partial^2 \phi}{\partial t^2} &= c^2 \Delta \phi \quad , \quad (r, \theta, z) \in \Omega, \quad t > 0, \\ \nabla \phi \cdot \hat{n} &= 0 \quad , \quad (r, \theta, z) \in \Gamma, \quad t > 0, \\ \frac{\partial \phi}{\partial z}(t, r, \theta, 0) &= -\frac{\partial w}{\partial t}(t, r, \theta) \quad , \quad (r, \theta) \in \Gamma_0, \quad t > 0, \\ \rho h \frac{\partial^2 w}{\partial t^2} - \frac{\partial^2 M_r}{\partial r^2} - \frac{2}{r} \frac{\partial M_r}{\partial r} + \frac{1}{r} \frac{\partial M_\theta}{\partial r} - \frac{2}{r} \frac{\partial^2 M_{r\theta}}{\partial r \partial \theta} - \frac{2}{r^2} \frac{\partial M_{r\theta}}{\partial \theta} - \frac{1}{r^2} \frac{\partial^2 M_\theta}{\partial \theta^2} \\ &= \frac{-\partial^2 (M_r)_{pe}}{\partial r^2} - \frac{2}{r} \frac{\partial (M_r)_{pe}}{\partial r} + \frac{1}{r} \frac{\partial (M_\theta)_{pe}}{\partial r} - \frac{1}{r^2} \frac{\partial^2 (M_\theta)_{pe}}{\partial \theta^2} \\ &\quad - \rho_f \frac{\partial \phi}{\partial t}(t, r, \theta, 0) + f(t, r, \theta), \\ w(t, R, \theta) &= \frac{\partial w}{\partial r}(t, R, \theta) = 0 \end{aligned} \tag{2.5}$$

with initial conditions

$$\begin{aligned}\phi(0, r, \theta, z) &= \phi_0(r, \theta, z) \quad , \quad w(0, r, \theta) = w_0(r, \theta) \quad , \\ \frac{\partial \phi}{\partial t}(0, r, \theta, z) &= \phi_1(r, \theta, z) \quad , \quad \frac{\partial w}{\partial t}(0, r, \theta) = w_1(r, \theta) \quad .\end{aligned}$$

It is noted that in this form, moments are differentiated in the plate component. Because the moments are discontinuous due to piecewise constant material parameters and control inputs, this leads to regularity problems associated with the differentiation of a Dirac delta ‘function’. To avoid ensuing difficulties with the differentiation and to reduce smoothness requirements on approximating bases, it is advantageous to reformulate the problem in a corresponding weak or variational form.

Weak Formulation of System Model

To provide classes of functions which are considered when defining a variational form of the problem, we consider the state space $X = \bar{L}^2(\Omega) \times L^2(\Gamma_0)$ and space of test functions $V = \bar{H}^1(\Omega) \times H_0^2(\Gamma_0)$ where $H_0^2(\Gamma_0) = \{\psi \in H^2(\Gamma_0) : \psi = \frac{\partial \psi}{\partial r} = 0 \text{ at } r = R\}$. Here $\bar{L}^2(\Omega)$ and $\bar{H}^1(\Omega)$ are the quotient spaces of $L^2(\Omega)$ and $H^1(\Omega)$ over the constant functions (the use of these spaces is due to the fact that the potentials are determined only up to a constant).

As detailed in [7, 22], an appropriate variational form of the coupled system model is

$$\begin{aligned}& \int_{\Omega} \frac{\rho_f}{c^2} \frac{\partial^2 \phi}{\partial t^2} \bar{\xi} d\omega + \int_{\Omega} \rho_f \nabla \phi \cdot \nabla \bar{\xi} d\omega \\& + \int_{\Gamma_0} \rho h \frac{\partial^2 w}{\partial t^2} \bar{\eta} d\gamma - \int_{\Gamma_0} M_r \frac{\partial^2 \bar{\eta}}{\partial r^2} d\gamma - \int_{\Gamma_0} \frac{1}{r} M_{r\theta} \frac{\partial \bar{\eta}}{\partial r} d\gamma - \int_{\Gamma_0} \frac{1}{r^2} M_{r\theta} \frac{\partial^2 \bar{\eta}}{\partial \theta^2} d\gamma \\& - 2 \int_{\Gamma_0} \frac{1}{r} M_{r\theta} \frac{\partial^2 \bar{\eta}}{\partial r \partial \theta} d\gamma + 2 \int_{\Gamma_0} \frac{1}{r^2} M_{r\theta} \frac{\partial \bar{\eta}}{\partial \theta} d\gamma \\& + \int_{\Gamma_0} \rho_f \left(\frac{\partial \phi}{\partial t} \bar{\eta} - \frac{\partial w}{\partial t} \bar{\xi} \right) d\gamma \\& = \int_{\Gamma_0} \sum_{i=1}^s \mathcal{K}_i^B u_i(t) \bar{\nabla}^2 \eta \chi_i(r, \theta) d\gamma + \int_{\Gamma_0} f \bar{\eta} d\gamma\end{aligned} \tag{2.6}$$

for all test functions $(\xi, \eta) \in V$. In this formulation, $d\omega = r dr d\theta dz$ and $d\gamma = r dr d\theta$ while the overbars in (2.6) denote complex conjugates. An abstract formulation for this model, which leads to well-posedness results, is given in [4, 7, 22].

2.2 Spatial Approximation

To obtain a time-dependent ODE system suitable for simulations, parameter estimation and control, a semidiscretization of the plate and acoustic states was performed. As detailed in

[22], appropriate Galerkin approximations of the displacement and potential are given by

$$w^{\mathcal{N}}(t, r, \theta) = \sum_{j=1}^{\mathcal{N}} w_j^{\mathcal{N}}(t) B_j^{\mathcal{N}}(r, \theta)$$

$$\phi^{\mathcal{M}}(t, r, \theta, z) = \sum_{j=1}^{\mathcal{M}} \phi_j^{\mathcal{M}}(t) B_j^{\mathcal{M}}(r, \theta, z).$$

The basis $\{B_j^{\mathcal{N}}(r, \theta)\}$ is constructed from modified cubic splines in r combined with periodic Fourier components in θ while modified Legendre polynomials in r and z were combined with Fourier components in θ to obtain $\{B_j^{\mathcal{M}}(r, \theta, z)\}$. In all examples which follow, a total of $\mathcal{M} = 99$ and $\mathcal{N} = 12$ basis functions were employed.

Projection of the system (2.6) onto the finite dimensional subspace spanned by the bases yields a $\mathcal{P} = 2(\mathcal{M} + \mathcal{N})$ dimensional ODE system

$$M^{\mathcal{P}} \dot{x}^{\mathcal{P}}(t) = \tilde{A}^{\mathcal{P}} x^{\mathcal{P}}(t) + \tilde{B}^{\mathcal{P}} u(t) + \tilde{F}^{\mathcal{P}}(t)$$

$$M^{\mathcal{P}} x^{\mathcal{P}}(0) = \tilde{x}_0^{\mathcal{P}}. \quad (2.7)$$

The vector $x^{\mathcal{P}}(t)$ has the form $x^{\mathcal{P}}(t) = [\varphi(t), \vartheta(t), \dot{\varphi}(t), \dot{\vartheta}(t)]^T$ where $\varphi(t) = [\phi_1^{\mathcal{M}}(t), \dots, \phi_{\mathcal{M}}^{\mathcal{M}}(t)]$ and $\vartheta(t) = [w_1^{\mathcal{N}}(t), \dots, w_{\mathcal{N}}^{\mathcal{N}}(t)]$ contain the generalized Fourier coefficients for the approximate acoustic potential and plate displacement, respectively. The vector $u(t) = [u_1(t), \dots, u_s(t)]^T$ contains the s patch input variables. The system matrices and vectors have the form

$$M^{\mathcal{P}} = \left[\begin{array}{c|c} K_A & \\ \hline & K_P \\ \hline & M_A \\ & M_P \end{array} \right], \quad \tilde{A}^{\mathcal{P}} = \left[\begin{array}{c|c} & K_A \\ \hline & K_P \\ \hline -K_A & -A_{c1} \\ & -A_{c2} \quad -C_P \end{array} \right] \quad (2.8)$$

and

$$\tilde{B}^{\mathcal{P}} = [0, 0, 0, \hat{B}]^T, \quad \tilde{F}^{\mathcal{P}}(t) = [0, 0, 0, \hat{g}(t)]^T.$$

The vector $\tilde{x}_0^{\mathcal{P}}$ contains the projections of the initial values into the approximating finite dimensional subspaces while \hat{B} and $\hat{g}(t)$ contain the input terms. The component matrices M_P, K_P and C_P are the mass, stiffness and damping matrices for the *isolated* plate while M_A and K_A denote the mass and stiffness matrices which arise when approximating the *uncoupled* wave equation with Neumann boundary conditions on a cylindrical domain (see [22] for details regarding these formulations). Contributions due to the coupling are contained in the matrices

$$[A_{c1}]_{i,\ell} = - \int_{\Gamma_0} \rho_f B_{\ell}^{\mathcal{N}} \overline{B_i^{\mathcal{M}}} d\gamma, \quad [A_{c2}]_{\ell,i} = \int_{\Gamma_0} \rho_f B_i^{\mathcal{M}} \overline{B_{\ell}^{\mathcal{N}}} d\gamma$$

where the index ranges are $i = 1, \dots, \mathcal{M}$ and $\ell = 1, \dots, \mathcal{N}$.

Multiplication by the inverted system mass matrix then yields the equivalent Cauchy system

$$\dot{x}^{\mathcal{P}}(t) = A^{\mathcal{P}} x^{\mathcal{P}}(t) + B^{\mathcal{P}} u(t) + F^{\mathcal{P}}(t)$$

$$x^{\mathcal{P}}(0) = x_0^{\mathcal{P}}. \quad (2.9)$$

Observed System

In control applications, one typically has available only a limited number of state observations. Hence for implementation purpose, a finite dimensional observation operator C^P yielding approximate state observations

$$y^P(t) = C^P x^P(t) \quad (2.10)$$

must be developed. It is assumed here that a total of m measurements are made at the points

$$\left. \begin{array}{ll} \text{Potential: } \omega_{i_\phi}, & i_\phi = 1, \dots, N_\phi \\ \text{Displacement: } \gamma_{i_w}, & i_w = 1, \dots, N_w \\ \text{Pressure: } \omega_{i_p}, & i_p = 1, \dots, N_p \\ \text{Velocity: } \gamma_{i_v}, & i_v = 1, \dots, N_v \end{array} \right\} \Rightarrow m = N_\phi + N_w + N_p + N_v. \quad (2.11)$$

An appropriate observation operator is then

$$C^P = \begin{bmatrix} C_\phi & 0 & 0 & 0 \\ 0 & C_w & 0 & 0 \\ 0 & 0 & C_p & 0 \\ 0 & 0 & 0 & C_v \end{bmatrix}, \quad \begin{array}{l} C_\phi \in \mathbb{R}^{N_\phi \times \mathcal{M}} \\ C_w \in \mathbb{R}^{N_w \times \mathcal{N}} \\ C_p \in \mathbb{R}^{N_p \times \mathcal{M}} \\ C_v \in \mathbb{R}^{N_v \times \mathcal{N}} \end{array} \quad (2.12)$$

where

$$\begin{aligned} [C_\phi]_{i_\phi, k} &= B_k^{\mathcal{M}}(\omega_{i_\phi}) = \int_{\Omega} \delta(\omega - \omega_{i_\phi}) B_k^{\mathcal{M}} d\omega \\ [C_w]_{i_w, k} &= B_k^{\mathcal{N}}(\gamma_{i_w}) = \int_{\Gamma_0} \delta(\gamma - \gamma_{i_w}) B_k^{\mathcal{N}} d\gamma \\ [C_p]_{i_p, k} &= B_k^{\mathcal{M}}(\omega_{i_p}) = \int_{\Omega} \rho_f \delta(\omega - \omega_{i_p}) B_k^{\mathcal{M}} d\omega \\ [C_v]_{i_v, k} &= B_k^{\mathcal{N}}(\gamma_{i_v}) = \int_{\Gamma_0} \delta(\gamma - \gamma_{i_v}) B_k^{\mathcal{N}} d\gamma. \end{aligned}$$

Note that the i_ϕ^{th} observation of the approximate potential is given by

$$[y(t)]_{i_\phi} = [C_\phi \varphi(t)]_{i_\phi} = \phi^{\mathcal{M}}(t, \omega_{i_\phi})$$

with analogous expressions for the observed displacement, pressure and velocity.

Unmodeled Dynamics

The system (2.9) provides an approximation of the structural acoustic and electromechanical components of the experimental system described at the beginning of this section. It ignores, however, the electrical effects of the necessary control circuitry (e.g., amplifiers, filters, A/D and D/A converters) and unmodeled physical contributions which are unavoidable

in experimental systems. For example, the damping provided by the patches when the circuit is completed is not explicitly included in the model.

To incorporate such unmodeled effects, uncertainties in the form of additive random state perturbations are included in the model. With $\alpha_1(t), \dots, \alpha_4(t)$ taken as random variables on $[-.1, .1]$, this can be accomplished through the inclusion of a term

$$D^{\mathcal{P}}\eta^{\mathcal{P}}(t) \equiv \left[\begin{array}{c|c} 0 & 0 \\ \hline 0 & 0 \\ \hline -K_A & -A_{c1} \\ \hline -K_P & -A_{c2} \quad -C_P \end{array} \right] \left[\begin{array}{c} \alpha_1\varphi(t) \\ \alpha_2\vartheta(t) \\ \alpha_3\dot{\varphi}(t) \\ \alpha_4\dot{\vartheta}(t) \end{array} \right] \quad (2.13)$$

in the finite dimensional model (2.9). Note that this yields the coupled dynamic ODE system

$$\begin{aligned} M_A\ddot{\varphi}(t) + K_A[1 + \alpha_1(t)]\varphi(t) + A_{c1}[1 + \alpha_4(t)]\dot{\vartheta}(t) &= 0 \\ M_P\ddot{\vartheta}(t) + C_P[1 + \alpha_4(t)]\dot{\vartheta}(t) + K_P[1 + \alpha_2(t)]\vartheta(t) + A_{c2}[1 + \alpha_3(t)]\dot{\varphi}(t) &= \hat{B}u(t) + \hat{g}(t) \end{aligned} \quad (2.14)$$

which incorporates damping and stiffness uncertainties. While other choices for $D^{\mathcal{P}}$ exist [2, 10], this construction incorporates uncertainties at the constitutive level. It is further motivated by experimental results in [8] which demonstrate that while damping effects due to completed patch circuits are unmodeled, the effect is phenomenologically similar to the Kelvin-Voigt damping. This is exactly the manner through which damping uncertainties are incorporated in (2.13).

It is further assumed that errors proportional to the output are found in the observed data. To include these contributions, the observations are taken of the form

$$y^{\mathcal{P}}(t) = C^{\mathcal{P}}x^{\mathcal{P}}(t) + E^{\mathcal{P}}\eta(t)$$

where $[E^{\mathcal{P}}\eta(t)]_j = \hat{\alpha}_j(t)[C^{\mathcal{P}}x^{\mathcal{P}}(t)]_j$, $j = 1, \dots, m$. Here $\hat{\alpha}_j(t)$ is a random variable on $[-.1, .1]$.

To summarize, the observed system with state and measurement uncertainties is given by

$$\begin{aligned} \dot{x}^{\mathcal{P}}(t) &= A^{\mathcal{P}}x^{\mathcal{P}}(t) + B^{\mathcal{P}}u(t) + D^{\mathcal{P}}\eta(t) + F^{\mathcal{P}}(t) \\ y^{\mathcal{P}}(t) &= C^{\mathcal{P}}x^{\mathcal{P}}(t) + E^{\mathcal{P}}\eta(t). \end{aligned} \quad (2.15)$$

2.3 Control Formulation

We briefly summarize here the methodology for the H^∞ /MinMax periodic control of the finite dimensional structural acoustic system (see [2] for details). It is assumed that the only exogenous moments and forces being applied to the plate are periodic forces having a period τ ; hence $F(0) = F(\tau)$ in (2.15). Note that in accordance with usual finite dimensional control convention, we will drop all superscripts throughout the remainder of this work. It can be assumed throughout that the system dimension is $\mathcal{P} = 2(\mathcal{M} + \mathcal{N})$.

Full State Feedback

For the case with *full state* information, the system to be controlled is

$$\begin{aligned}\dot{x}(t) &= Ax(t) + Bu(t) + D\eta(t) + F(t) \\ x(0) &= x(\tau).\end{aligned}\tag{2.16}$$

The performance output $z(t) \in Z$ is given by

$$z(t) = Hx(t) + Gu(t),$$

where Z is a performance output space (see [19, 23]). For the finite dimensional approximate system, the problem of determining a controlling voltage can then be posed as the problem of finding $u \in L^2(0, \tau; U)$ which minimizes the steady-state disturbance-augmented functional

$$J(u) = \int_0^\tau \left\{ \langle Qx(t), x(t) \rangle_{\mathbb{R}^p} + \langle Ru(t), u(t) \rangle_{\mathbb{R}^s} - \gamma^2 |\eta(t)|_W^2 \right\} dt$$

where $x(t)$ solves (2.16), $R = G^T G$ is an $s \times s$ diagonal matrix containing weights which penalize overly large voltages to the patches [1], and W denotes the space in which disturbances evolve. An appropriate choice for the nonnegative matrix $Q = H^T H$, which stems from energy considerations, is a diagonal matrix multiple of the mass matrix in (2.7) (see [5]). Here $\gamma \in \mathbb{R}$ is a fixed positive constant which is a design parameter to be chosen as small as possible. In this case, the H^∞ norm of the closed loop disturbance to performance output transfer function from $\eta(\cdot)$ to $z(\cdot)$ is bounded above by γ .

Under suitable conditions (see [14]), optimal control theory can then be used to show that the optimal controlling voltage is given by

$$u(t) = -Kx(t) + R^{-1}B^T r(t)\tag{2.17}$$

where $K = R^{-1}B^T \Pi$ and Π is the unique nonnegative self adjoint solution to the algebraic Riccati equation

$$A^T \Pi + \Pi A - \Pi \left(BR^{-1}B^T - \frac{1}{\gamma^2} DD^T \right) \Pi + Q = 0.$$

The tracking component $r(t)$ solves the adjoint equation

$$\begin{aligned}\dot{r}(t) &= - \left[A - \left(BR^{-1}B^T - \frac{1}{\gamma^2} DD^T \right) \Pi \right]^T r(t) + \Pi F(t) \\ r(0) &= r(\tau).\end{aligned}\tag{2.18}$$

Output Feedback

The feedback law (2.17) is idealized in the sense that it requires knowledge of the full state (displacement, velocity, potential and pressure) which, using current instrumentation, is not possible. Instead, one typically has available measurements at a discrete number of points

(see (2.10)). From these observations y , the state is reconstructed or estimated by solving the MinMax state estimator equation

$$\begin{aligned}\dot{\hat{x}}(t) = & \left[A - F_c C - BK + \frac{1}{\gamma^2} DD^T \Pi \right] \hat{x}(t) + F_c y(t) \\ & + F(t) + \left(BR^{-1} B^T - \frac{1}{\gamma^2} DD^T \right) r(t) \\ \hat{x}(0) = & \hat{x}(\tau)\end{aligned}\tag{2.19}$$

(see [1, 2, 10, 14]). The observer gain F_c has a form similar to that of the feedback gain K and is given by $F_c = (I - \frac{1}{\gamma^2} \Sigma \Pi)^{-1} \Sigma C^T \mathcal{N}_e^{-1}$. Here \mathcal{N}_e is a design matrix which is related to the effect of noise in the data and Σ solves a second algebraic Riccati equation

$$A\Sigma + \Sigma A^T - \Sigma \left(C^T \mathcal{N}_e^{-1} C - \frac{1}{\gamma^2} Q \right) \Sigma + DD^T = 0.\tag{2.20}$$

In addition to the self adjointness and non-negativity of the matrices Π and Σ , a supplementary condition is typically imposed, namely the boundedness of the spectral radius of $\Sigma \Pi$ by γ^2 (see [1, 19, 23]). This latter condition can be expressed as

$$\rho_{sp}(\Sigma \Pi) < \gamma^2.$$

Once a state estimate $\hat{x}(t)$ is obtained, the controlling voltage is given by

$$u(t) = -K\hat{x}(t) + R^{-1}B^T r(t)\tag{2.21}$$

where $r(t)$ is again the unique τ -periodic solution of the adjoint or tracking equation (2.18).

3 Open Loop Simulations

To illustrate the effects of coupling and the manner through which the plate and acoustic components contribute to the coupled system dynamics, we summarize here characteristic open loop dynamics for the system. The dimensions for the system were chosen to be compatible with those of the experimental cylinder at NASA Langley Research Center which has length $\ell = 1.067\text{ m}$ (42") and radius $R = 0.229\text{ m}$ (9"). The end-mounted plate has thickness $h = 0.00127\text{ m}$ (0.05") with a pair of centered piezoceramic patches with respective thickness and radius $h_{pe} = 0.00018\text{ m}$ (0.007") and $R_{pe} = 0.019\text{ m}$ (0.75"). These values were then used for the simulations reported here. The physical parameters for the simulations are summarized in Table 1. As reported in [8], these values are also consistent with physical parameters for the experimental setup.

Throughout this section, control inputs are excluded ($u(t) = 0$) and impact-like spatial and acoustic inputs are used to generate transient system responses. A comparison of natural frequencies is then used to quantify the contributions of the structural and acoustic components and the two coupling mechanisms modeled by force (pressure) and velocity balancing.

To provide a baseline for comparison, natural frequencies for the *isolated* plate and acoustic field are summarized in Table 2. As detailed in [7, 22], where the full set of frequencies

are provided, the plate frequencies were calculated under the assumption of no damping ($c_D = 0$) while the acoustic frequencies were calculated under the assumption of fully Neumann boundary conditions.

As discussed in Section 2, force balancing is used to incorporate the acoustic effects on the structure; this leads to a pressure input term in the modeling acoustic equation. Velocity balancing incorporates the converse coupling mechanism through which energy is transmitted from the structure to the acoustic field. In terms of the component matrices in (2.7), these coupling components enter as input terms in the vector equations

$$\begin{aligned} M_A \ddot{\varphi}(t) + K_A \varphi(t) &= -A_{c1} \dot{\vartheta}(t) + F_M g(t) \\ M_P \ddot{\vartheta}(t) + C_P \dot{\vartheta}(t) + K_P \vartheta(t) &= -A_{c2} \dot{\varphi}(t) + F_N f(t) \end{aligned} \quad (3.1)$$

(compare with (2.14)).

Structure			Acoustic Cavity	
Parameter	Plate	Plate + Pzt	Parameter	Cavity
$\rho \cdot \text{Thickness} \text{ (kg/m}^2\text{)}$	3.429	3.489	$\rho_f \text{ (kg/m}^3\text{)}$	1.21
$D \text{ (N} \cdot \text{m)}$	13.601	13.901		
$c_D \text{ (N} \cdot \text{m} \cdot \text{sec)}$	1.150-4	2.250-4		
ν	.33	.32		
$K^B \text{ (N/V)}$.027		
			c (m/sec)	343

Table 1. Physical parameters for the structure and acoustic cavity.

Plate (f_{mn})		Wave (f_{mnp})			
(0,0)	62.0	(0,0,1)	160.8	(0,1,0)	915.0
(0,1)	241.2	(0,0,2)	321.5	(0,1,1)	929.0
(0,2)	540.5	(0,0,3)	482.3	(0,1,2)	969.9
(0,3)	959.5	(0,0,4)	643.0		
		(0,0,5)	803.8		
		(0,0,6)	964.6		

Table 2. Axisymmetric natural frequencies for the *isolated* and *undamped* plate and cavity (in hertz). The cavity mode (m, n, p) , corresponding to frequency f_{mnp} , has m nodal lines in θ , n nodal circles in r and p nodal lines z (similarly for plate modes).

The vectors $F_M g(t)$ and $F_N f(t)$ incorporate the exogenous input to the cavity and plate, respectively. For an impact at time $t = t_0$ applied at the plate point (r_0, θ_0) , the components of $F_N f(t)$ are given by

$$\begin{aligned} [F_N f(t)]_k &= \delta(t - t_0) \int_{\Gamma_0} \delta(r - r_0, \theta - \theta_0) B_k^N d\gamma \\ &= \delta(t - t_0) B_k^N(r_0, \theta_0) \end{aligned}$$

with a similar expression for the acoustic input. Note that one can consider $g(t) \equiv 0$ if no acoustic input is present as is the case in the coupled structural acoustic control problem. In all examples here, plate impacts are at $(r, \theta) = (0, 0)$ while cavity impacts are at $(r, \theta, z) = (0, 0, \ell/3)$.

By considering various coupling combinations (e.g., $A_{c1} \equiv 0$ eliminates the coupling mechanism through which energy is transmitted from the plate to the cavity) and force inputs $f(t), g(t)$, the effects of the two coupling mechanisms were isolated. The six coupling/input combinations are depicted in Figure 2 and are summarized below.

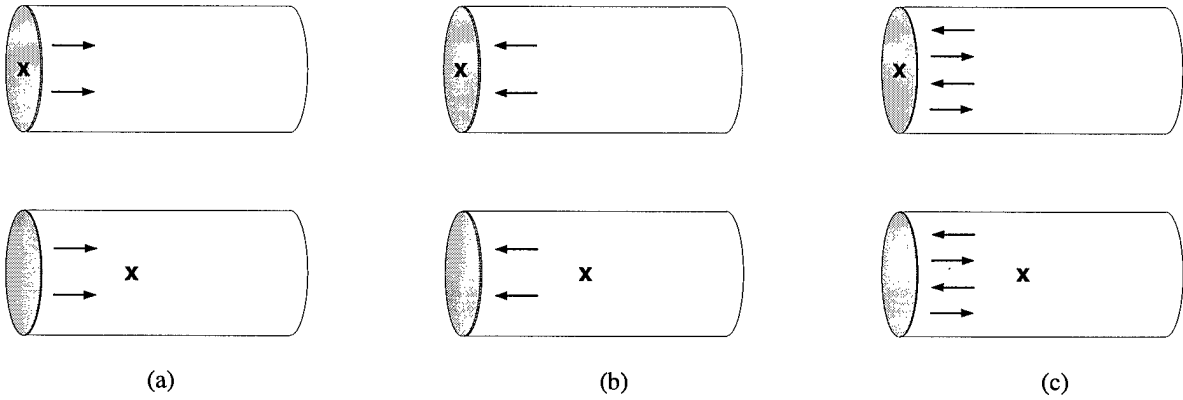


Figure 2. Coupling combinations with plate and acoustic impulse forces at the point \mathbf{x} ; (a) Coupling from structure to field; (b) Coupling from field to structure; (c) Full structural acoustic coupling.

Case (i): Coupling from Structure to Field

To illustrate the case in which coupling from the structure to the acoustic field is incorporated in the model but energy transfer from the field to the structure is neglected, we let $A_{c2} \equiv 0$ in (3.1) and (2.8). This case is depicted in Figure 2a. Note that the exogenous force $F_M g(t)$ and velocity coupling provide input to the cavity while the only input to the plate is provided by the exogenous force $F_N f(t)$.

Consider first the force choices $g(t) = 0, f(t) = \delta(t - t_0)$ which models an impact to the plate with no exogenous force to the cavity. Because the plate is unaffected by the acoustic field in this case, natural frequencies measured on the plate will be close to those summarized

in Table 2 with differences due only to the Kelvin-Voigt damping. The structure acts as an input to the cavity with frequencies governed by the harmonics of the plate. Hence both plate and wave frequencies will be measured in the cavity. The frequencies obtained via (2.7) at the plate point $p_1 = (0, 0)$ and cavity point $c_2 = (0, 0, .35)$ depicted in Figure 3 are summarized in Table 3. Frequencies calculated at the plate point are indicated in the table by p while c denotes frequencies measured at c_2 . It should be noted that to within the sampling resolution, the frequencies calculated at both points agree with those for the isolated components which are summarized in Table 2. Furthermore, Table 3 illustrates the transmission of plate frequencies into the cavity.

The conclusion for general structural acoustic systems will be similar. The incorporation of *only* the velocity coupling in the model will lead to a system response similar to that of the components with structural frequencies propagated into the acoustic field. This type of model might be useful if considering far field acoustics generated by a vibrating structure (e.g., transformer). As illustrated in Case (iii), however, it may provide inaccurate system frequencies in applications in which the acoustic oscillations couple back to the structure.

The second choice $g(t) = \delta(t - t_0)$, $f(t) = 0$ models an impact in the cavity with no exogenous force to the plate. The purely cavity frequencies summarized in Table 2 will be present at the cavity point c_2 . No response will be noted on the plate since the coupling between the field and plate is neglected in this case.

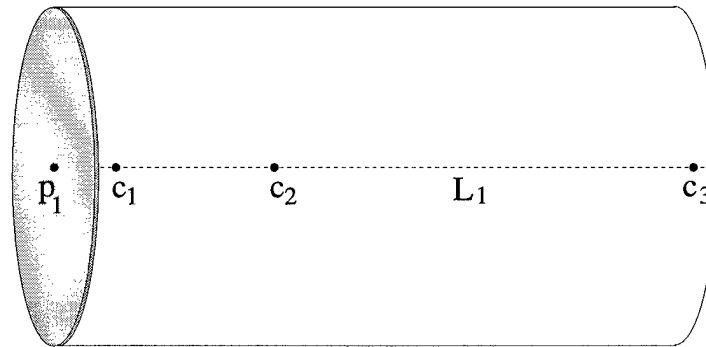


Figure 3. The structural acoustic system with evaluation points $p_1 = (0, 0)$, $c_1 = (0, 0.05)$, $c_2 = (0, 0, .35)$, $c_4 = (0, 0, 1.0)$ and evaluation line L_1 .

Natural System Frequencies					
p,c	62.0	c	160.8	c	915.4
p,c	241.2	c	321.5	c	928.1
p,c	540.5	c	482.3	c	969.8
p	959.5	c	643.7		
		c	806.6		

Table 3. System frequencies obtained with $A_{c2} \equiv 0$; p : frequencies observed at the plate point $p_1 = (0, 0)$, c : frequencies observed at the cavity point $c_2 = (0, 0, .35)$.

Case (ii): Coupling from Field to Structure

This case can be quantified by considering $A_{c1} \equiv 0$ in (2.8). As shown in (3.1) and depicted in Figure 2b, the model in this case incorporates the acoustic influence upon the structure but neglects structural influence upon the field. The dynamics can be predicted from those observed in Case (i) with the opposite mechanism. The acoustic frequencies are propagated to the structure when $g(t) = \delta(t - t_0)$, $f(t) = 0$ with both sets close to the those of the isolated components (the only deviation is a slight shift in the structural frequencies due to the Kelvin-Voigt damping). This model will be accurate *only* for systems in which the field strongly drives the structure with negligible feedback from the structure to the field.

Case (iii): Full Coupling between Field and Structure

The case of primary interest for the system considered here is that in which both coupling mechanisms are incorporated in the system model. Hence both the matrix A_{c1} (velocity coupling) and matrix A_{c2} (pressure coupling) are included in the ODE system (2.8) or (3.1).

System frequencies for this case are summarized in Table 4. A comparison between these results and corresponding frequencies for the uncoupled plate and acoustic field (see Table 2) indicates that while the system response reflects the structural and acoustic components, the system frequencies are shifted from those of the components due to the coupling. The three system frequencies corresponding to the plate component (59.5, 239.5, 538.2 Hz) are lower than the corresponding frequencies of the isolated plate. Thus the coupled acoustic field effectively mass loads the structure. The remaining system frequencies correspond to the acoustic component. They are higher than those for the isolated wave fields which indicates that the coupling of the plate to the acoustic field provides a stiffening effect to the field. For the geometry investigated here, we observe frequency shifts of approximately 2.5 Hz ($\approx 5\%$) for lower frequencies and 3 to 4 Hz ($\approx 1\%$ to 2%) for higher frequencies. Hence in many applications, the uncoupled systems will provide sufficient modal information.

However, for many systems which are closed in the sense that both acoustic/structure and structure/acoustic interactions are present, both mechanisms may need to be incorporated in the model to accurately match dynamics. Omission of either mechanism will lead to model frequencies which match those of the isolated components but may *not* match those of the actual coupled system. Employment of a model which neglects coupling components in a PDE-based controller can lead to decreased control authority. If the neglected coupling is significant, the controller will be destabilized by the ensuing frequency inaccuracies.

Natural System Frequencies					
p,c	59.5	p,c	163.4	c	915.6
p,c	239.5	p,c	324.1	p,c	929.3
p,c	538.2	p,c	483.1	p,c	971.0
		p,c	645.2		
		p,c	807.5		

Table 4. System frequencies obtained with full structural acoustic coupling conditions; p : frequencies observed at the plate point $p_1 = (0, 0)$, c : frequencies observed at the cavity point $c_2 = (0, 0, .35)$.

4 Closed Loop Simulations—Short Cylinder

For compensator design, the spatially discretized model (2.15) with full structural acoustic coupling was considered. The performances of the full state H^∞ /MinMax feedback control, output feedback MinMax control and LQG feedback control (Kalman filter) were then compared with open loop system responses for a variety of sensor configurations and geometries. This provided a means of evaluating and utilizing the coupling in the model-based compensator.

To illustrate, two geometries for the structural acoustic system were considered. For the first, dimensions consistent with those of the experimental chamber in the Acoustics Division, NASA Langley Research Center were used (see the discussion in Section 3 and Table 1). This provided simulation results which can be used to predict experimental dynamics and guide experiments involving that setup. The numerical results for this geometry are reported in this section. The second geometry involves an acoustic chamber whose length is significantly longer than the diameter of the vibrating plate. This illustrates the manner through which the acoustic wave equation describes the effective physical delays due to relatively slow wave speeds. It also indicates controllability issues which must be considered when designing controllers for such systems. Results for this geometry are summarized in Section 5.

The exogenous force to the plate was taken to be

$$f(t) = 28.8[\sin(2\pi 170t) + \sin(2\pi 330t) + \sin(2\pi 100t) + \sin(2\pi 250t)]. \quad (4.1)$$

This models a plane acoustic wave with an rms sound pressure level of 126 dB. This excites a combination of modes since the first two frequencies (170 Hz, 330 Hz) couple readily with cavity-like modes while the latter two frequencies strongly affect plate-like frequencies (see Tables 2 and 4).

Consideration of the control laws outlined in Section 2.3 indicates several design parameters which can be used to weight input and output values as well as various states and sensors. The specific design of the model uncertainty matrix D and output uncertainty matrix E also can be modified according to the application. Furthermore, the parameter γ which bounds the H^∞ norm of the transfer function from disturbance to performance output can be tuned to improve performance.

Various criteria are considered when choosing these design parameters. These include overall attenuation levels, control magnitude (overly large voltages will destroy the patches), conditioning of Riccati solutions and spectrum stability of the closed loop system. Many of these issues are addressed in [3] and the reader is referred to that reference for a general discussion of these design criteria. Reference [4] contains details regarding the specific choices for these simulations.

The design criteria involving the state, observation and control weights, and MinMax parameter γ , arise from the formulation of the control law rather than the physics of the problem. The placement and number of sensors and actuators, however, is a design criterion which is directly related to the physics. As mentioned previously, a pair of circular, centered piezoceramic patches are employed as actuators in the experimental system. These actuators are glued to the plate and are considered as permanent throughout both experiments and simulations. The use of this single pair proved adequate for this geometry and axisymmetric force (4.1) but led to controllability problems in the long cylinder discussed in the next section.

The sensors are often more portable (unless piezoceramic patches or other permanently bonded materials are employed) and a variety of configurations were considered. Criteria which are considered when determining number and placement are hardware limitations (restricted number of input channels for data acquisition), physical constraints (sensors outside a transformer or submarine are unsuitable), Riccati solution conditioning etc. The hardware constraints limit the available number of sensors while physical constraints often make it advantageous to limit the types and placement of sensors. The ideal case is to eliminate the acoustic sensors entirely and use the model with coupling along with structural data to reconstruct the acoustic state.

For the simulations presented here, three sensor configurations were considered as summarized in Table 5. In all cases, the number of sensors measuring the potential was taken to be $N_\phi = 0$ in (2.11) when constructing the observation matrix (2.12). This is due to the fact that the potential is not a readily measured state.

For Compensator I, 5 microphone, 5 velocity, and 5 displacement measurements at the observation points

$$\begin{aligned}\omega_{1p} &= (0, 0, .0334) , & \gamma_{1w} &= \gamma_{1v} = (R/3, 0) \\ \omega_{2p} &= (R, 0, \ell/2) , & \gamma_{2w} &= \gamma_{2v} = (R/3, \pi) \\ \omega_{3p} &= (R, \pi, \ell/2) , & \gamma_{3w} &= \gamma_{3v} = (2R/3, \pi/2) \\ \omega_{4p} &= (R, \pi/2, \ell) , & \gamma_{4w} &= \gamma_{4v} = (2R/3, 7\pi/6) \\ \omega_{5p} &= (R, 3\pi/2, \ell) , & \gamma_{5w} &= \gamma_{5v} = (2R/3, 11\pi/6)\end{aligned}$$

were used for state reconstruction (see Figure 4). This implies that $N_p = N_w = N_v = 5$ in (2.12).

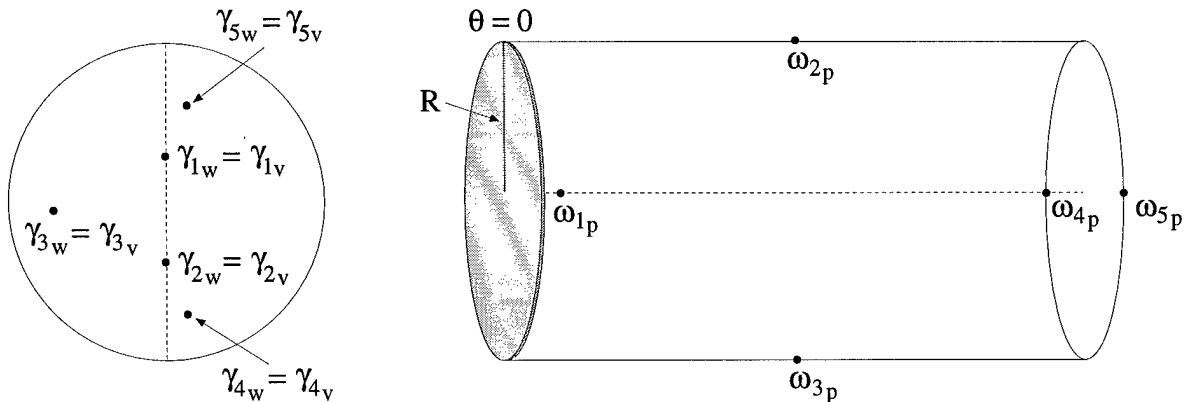


Figure 4. Pressure and plate observation points for the structural acoustic system.

Compensator II differs from Compensator I in the manner through which the microphone observation submatrix C_p is employed. For the calculation of the observer gain through solution of the observer Riccati equation (2.20), this submatrix was retained so that the full observation matrix C had dimension $(N_p + N_w + N_v) \times (2\mathcal{N} + \mathcal{M})$. For the calculation of the state output (2.15) and the state estimate $\hat{x}(t)$ solving (2.19), however, only plate

measurements were considered so $N_p = 0$ which results in a null submatrix C_p in (2.12). The acoustic sensors utilized in this manner are referred to as *virtual* microphones.

This second compensator is motivated by the goal of eliminating the acoustic sensors and utilizing the coupled model for state reconstruction using solely structural data. This is what is implemented in the state calculations (2.19). The motivation for including the pressure submatrix C_p when calculating the observer gain is the maintenance of conditioning for Riccati solutions, lower spectral radii and closed loop spectrum bounds. As illustrated in [4], solution of the observer Riccati equation (2.20) with solely structural observation components leads to unacceptable conditioning and spectral radii when computing observer gains.

Compensator III utilizes both virtual microphones and virtual displacement sensors so that the only physical data used when estimating the state are velocity measurements. This is motivated by physical constraints on structural sensors. Displacement measurements using proximity sensors are typically difficult to obtain whereas velocity measurements can be obtained using laser vibrometers or integration of accelerometer data. Nonzero initial conditions for the state estimator were employed in all three compensators. As detailed in [4], this permitted additional comparison between the performance of the three compensators.

The construction of a controller using virtual sensors provides a great deal of flexibility. In addition to permitting the design of controllers utilizing certain state measurements, it provides the capability for developing controllers designed for a variety of environments. The observation gains are computed using the full observation matrix in each case. The observer submatrices C_p, C_w, C_v can then be incorporated or omitted in the state estimator computations depending on the available data. This allows for some latitude in sensor location as well as the disabling (in the data collection process) of damaged or superfluous sensors. While heuristic in nature, the dual incorporation of the observation submatrices to accommodate virtual sensors proves an effective technique for reducing the number of physical sensors while maintaining the conditioning of the gain and observer matrices.

The final control laws considered are the full state H^∞ /MinMax controller (2.17) and the Kalman filter which results with $\gamma = \infty$. These two laws provide benchmarks against which to compare the H^∞ /MinMax output feedback controllers.

	Sensors			Sensor Components	Sensor Components
	Mics.	Disp.	Vel.	for Riccati Solution	for Control Computation
Compensator I	5	5	5	$N_p = N_w = N_v = 5$	$N_p = N_w = N_v = 5$
Compensator II	5 Virtual	5	5	$N_p = N_w = N_v = 5$	$N_p = 0, N_w = N_v = 5$
Compensator III	5 Virtual	5 Virtual	5	$N_p = N_w = N_v = 5$	$N_p = N_w = 0, N_v = 5$
Kalman Filter	5	5	5	$N_p = N_w = N_v = 5$	$N_p = N_w = N_v = 5$
H^∞ Control	Full State				

Table 5. Full state and output feedback control laws with sensor numbers.

Trajectories for the uncontrolled system and system controlled via the five control laws were computed over the time interval $[0, .16]$ with 0%, 5% and 10% relative noise added to the model and observations. The rms pressure values at the cavity points c_1, c_2, c_3 and the rms displacement at the plate center $p_1 = (0, 0)$ for the 5% noise case are summarized in Table 6. Time domain plots of the uncontrolled and controlled pressure at $c_1 = (0, 0, .05)$ are given in Figure 5 while the rms sound pressure values along the central axis L_1 (see Figure 3) are plotted in Figure 6.

As expected, the full state H^∞ /MinMax controller provides the best performance since it utilizes the most information. With 5% noise, it provides a 12.5 dB reduction at c_1 with equally significant reductions throughout the length of the cavity. The Kalman filter yields an 8.5 dB reduction at c_1 with performance less than the full state MinMax control due to the limited number of observations and the lack of robustness in the presence of noise. The three MinMax compensators yield 7-8 dB reductions at c_1 with similar performances throughout the cavity. In comparing the rms values and time plots of the three compensators, it is noted that the performance of Compensator I with measurements of pressure, displacement and velocity is only 1-2 dB better than that of Compensators II and III. Recall from Table 5 that Compensator III employs *only* 5 velocity sensors for the actual state reconstruction. The pre-computed gains and coupled model provide the remaining information required for accurate state estimation and control computation.

The global nature of the noise reduction should also be noted. Both time and rms plots illustrate that model-based controllers employing the structure-mounted actuator provide significant attenuation *throughout* the cavity.

These results demonstrate the possibility of obtaining very effective control attenuation using only structural observations with the coupled model used to estimate the structural and acoustic states. This is important in many interior field applications such as the structural acoustic system described here and crucial in exterior field applications (e.g., transformer or submarine) where acoustic measurements may be impossible to attain.

	Sound pressure level (dB)			Displacement (m)
	c_1	c_2	c_3	p_1
open loop	119.7	113.7	119.7	12.4×10^{-5}
MinMax full state	107.2	103.2	104.1	8.0×10^{-5}
Kalman filter (I)	111.3	105.9	110.9	8.0×10^{-5}
MinMax compensator (I)	111.3	105.9	110.9	8.0×10^{-5}
MinMax compensator (II)	112.8	106.9	112.3	8.0×10^{-5}
MinMax compensator (III)	112.8	106.9	112.3	8.0×10^{-5}

Table 6. Sound pressure levels and displacements (rms) in the presence of 5% noise.

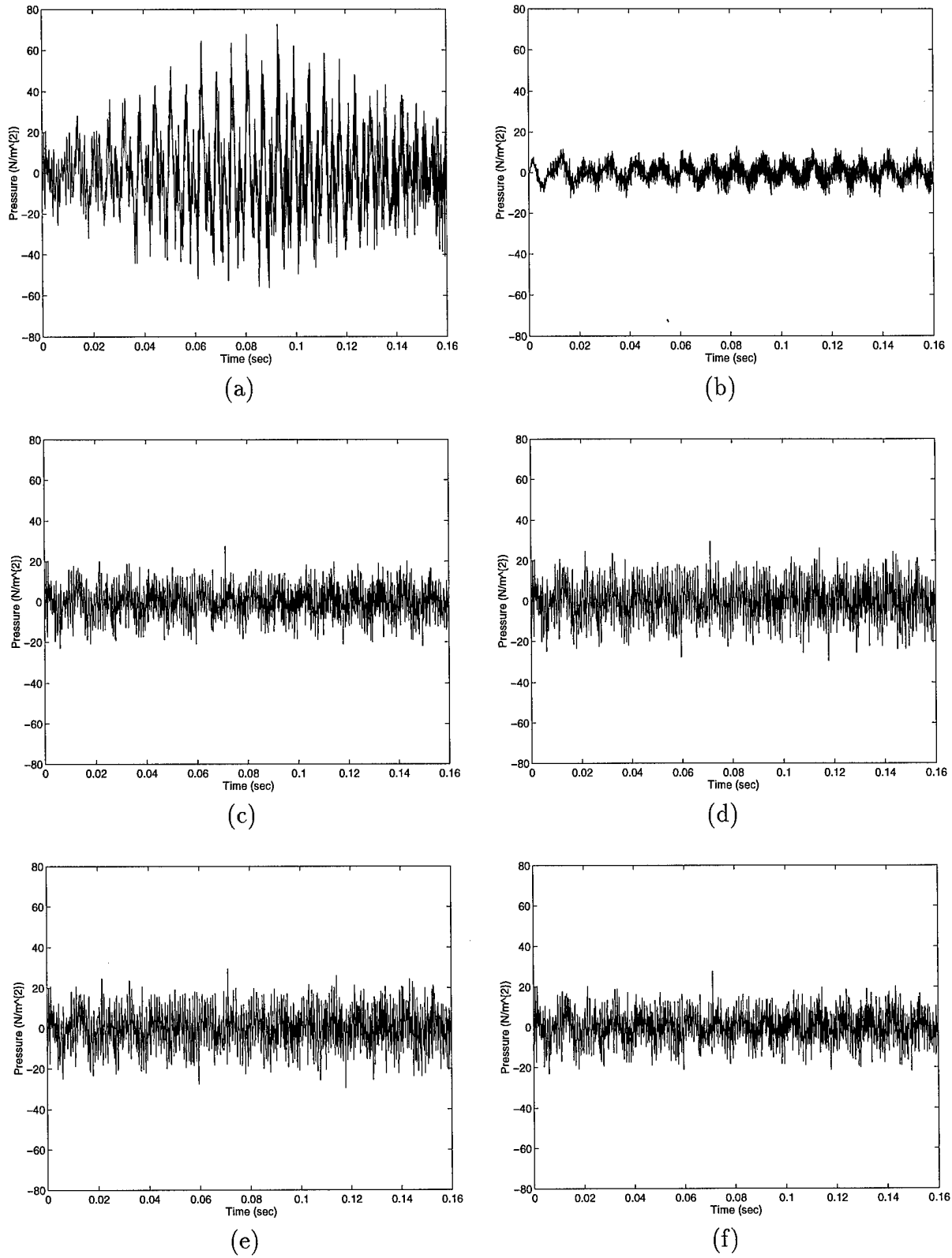


Figure 5. Time history of sound pressure level at $c_1 = (0, 0, 0.05)$ with 5% noise; (a) Open loop, (b) Full state MinMax controller, (c) MinMax compensator I, (d) MinMax compensator II, (e) MinMax compensator III, (f) Kalman filter.

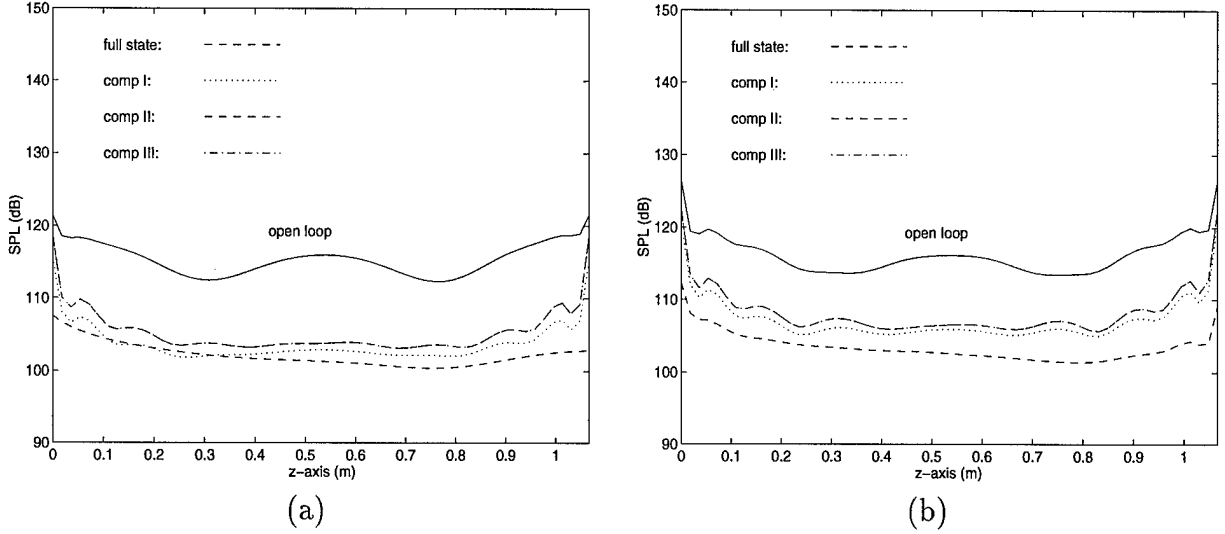


Figure 6. Sound pressure level along central z -axis L_1 over the time interval $[0, 0.16]$; (a) 0% noise, (b) 5% noise. Compensators II and III provide graphically identical attenuation.

5 Closed Loop Simulations – Long Cylinder

Two physical mechanisms that contribute significantly to the difficulty in controlling structure-borne noise are the structural acoustic coupling and the relatively slow wave speed in the acoustic field. The effects and utilization of the coupling have been described in previous sections and will be re-addressed in Section 6. The efficacy of using the dynamic wave model to incorporate the wave speed is illustrated here through consideration of a cylinder whose length is significantly larger than the end-mounted vibrating plate (see Figure 7a). Specifically, the plate has the same dimensions as that in previous sections while the length of the cylinder is now 3.206 m . This yields a cylindrical length to plate diameter ratio of 7 as compared to 2.33 in Section 4. The forcing function in (4.1) was again used to model a uniform periodic acoustic field driving the plate.

For these simulations, three patch configurations were considered as depicted in Figure 7b, c, d. Specifically, two pairs were circular ($r_1 = 0, r_2 = R/12$ and $r_1 = 0, r_2 = R/4$) and one was ringlike ($r_1 = R/3, r_2 = R/2$). The MinMax parameter choice $\gamma = 10$ provided an adequate balance between conditioning and stability.

For the full state feedback law (2.17), rms sound pressure levels along the axes

$$A1: (\theta = 0, r = 0, 0 \leq z \leq \ell)$$

$$A2: (\theta = 0, r = R/4, 0 \leq z \leq \ell)$$

$$A3: (\theta = 0, r = R/2, 0 \leq z \leq \ell)$$

$$A4: (\theta = 0, r = 3R/4, 0 \leq z \leq \ell)$$

(see Figure 7a) are plotted in Figure 8. In each case, it is noted that the small circular patch pair ($r_1 = 0, r_2 = R/12$) provides the least attenuation whereas the patch ring provides up to 30 dB attenuation. It is also noted that negligible attenuation is attained along the middle

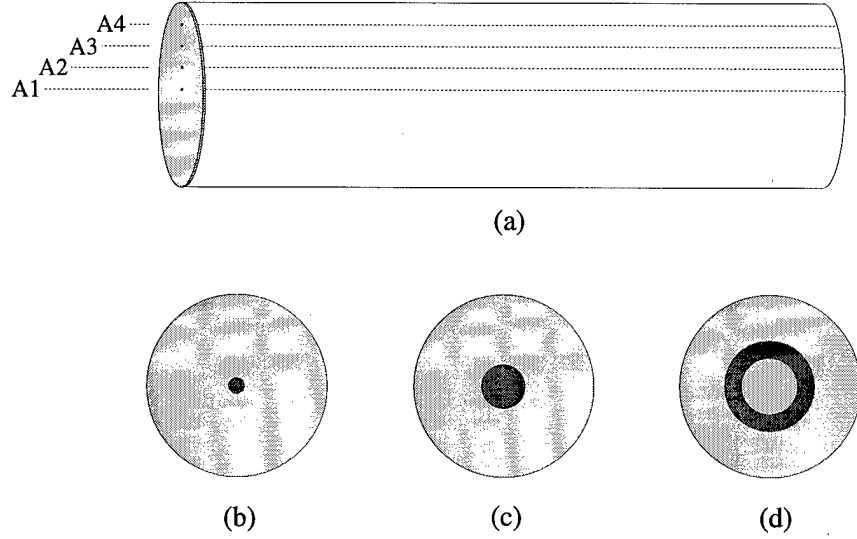


Figure 7. (a) The acoustic cavity with observation axes $1, \dots, 4$; (b) patch with radius $r = R/12$; (c) patch with radius $r = R/4$; (d) patch ring with $r_1 = R/4, r_2 = R/2$.

$1/3$ of the central axis. This illustrates a controllability issue which arises when utilizing a single patch pair in a system whose length is significantly longer than the driving plate. Hence while significant attenuation is achieved throughout most of the cavity, optimization issues concerning patch number and orientation should be investigated to attain global attenuation.

Similar results obtained with Compensators I and III described in Table 5 are plotted in Figure 9. The small patch having radius $R/12$ was employed as an actuator and rms sound pressure levels along axis 2 are reported in the figure. For both cases (0% and 5% noise), 10-12 dB reductions were obtained along this axis, even with Compensator III which employs only 5 velocity observations for state reconstruction. The tendencies along axes 3 and 4 are similar while the rms pressure along axis 1 still exhibits the central region with negligible control.

For both the full state feedback controller and the compensator, the information regarding propagation of the acoustic response is provided by the *dynamic* wave equation (2.1). Due to the low wave speed (343 m/sec), the time delay between the input of voltage to the patch and the acoustic response at a sensor is significant. If left unmodeled or uncompensated, this delay will destabilize a controller. This is one motivation for utilizing wave-based rather than modal-based controllers in many acoustic applications. As illustrated by the results in Figures 8 and 9, as well as the previous section, the use of a *dynamic* wave model very adequately accounts for the delay thus leading to strong attenuation for this system.

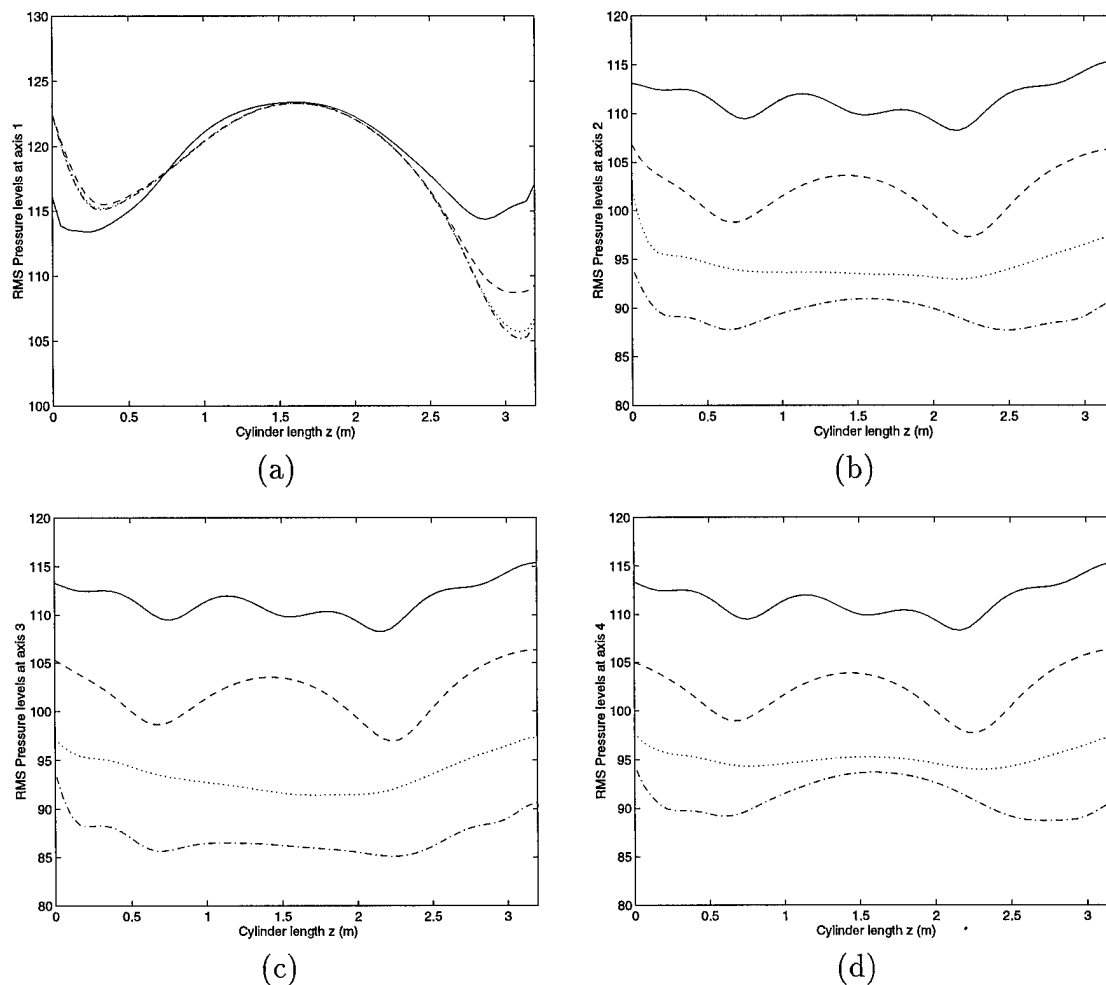


Figure 8. Root mean square (rms) sound pressure levels for 0% noise with full state feedback; — (Open loop), --- (Small circular patch), (Large circular patch), - . - . - (Patch ring); (a) Axis 1, (b) Axis 2, (c) Axis 3, (d) Axis 4.

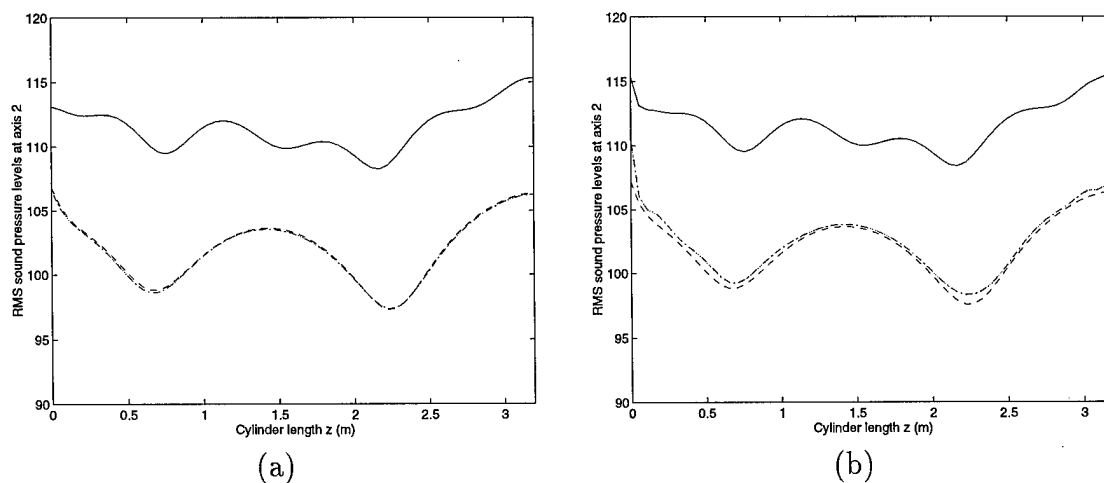


Figure 9. RMS sound pressure levels along axis 2 with small patch as actuator; — (Open loop), --- (Full state MinMax control), (MinMax compensator I), - . - . - (MinMax compensator III); (a) 0% noise, (b) 5% noise.

6 Closed Loop Simulations—Plate-based controller

The fact that structure-borne noise is generated by a vibrating structure makes it tempting to reduce the noise solely by controlling the structure. The example we consider in this section reinforces the tenet held by many acousticians that this strategy is not effective in general and should be used only for certain exogenous frequencies (see, for example, [13, 20]). It also illustrates the benefits of utilizing a compensator for the coupled system which employs only structural sensors (see Compensator III of Table 5) rather than a purely structural controller.

For the structural acoustic system in this work, a purely structural controller would be designed for the discretized plate model

$$\begin{bmatrix} K_P & 0 \\ 0 & M_P \end{bmatrix} \begin{bmatrix} \dot{\vartheta}(t) \\ \ddot{\vartheta}(t) \end{bmatrix} = \begin{bmatrix} 0 & K_P \\ -K_P & -C_P \end{bmatrix} \begin{bmatrix} \vartheta(t) \\ \dot{\vartheta}(t) \end{bmatrix} + \begin{bmatrix} 0 \\ \hat{B} \end{bmatrix} u(t) + \begin{bmatrix} 0 \\ \hat{g}(t) \end{bmatrix} + \hat{D}\eta(t)$$

where again, $\vartheta(t)$ contains the generalized Fourier coefficients for displacement and M_P, K_P and C_P are the mass, stiffness and damping matrices for the plate (see Section 2). The control, exogenous force and uncertainties are contained in $\hat{B}u(t), \hat{g}(t)$ and $\hat{D}\eta(t)$, respectively. The observation matrix for this case is

$$y(t) = \begin{bmatrix} C_w & 0 \\ 0 & C_v \end{bmatrix} \begin{bmatrix} \vartheta(t) \\ \dot{\vartheta}(t) \end{bmatrix}$$

with 5 displacement and velocity observations ($N_w = N_v = 5$).

Control results for the forcing functions $f_1(t) = \sin(130\pi t)$, $f_2(t) = \sin(330\pi t)$ using the plate-based compensator with $N_w = N_v = 5$ are reported in Tables 7 and 8. The first frequency couples effectively with the 59.5 Hz plate-like mode while $f_2(t)$ strongly drives the 163.4 Hz cavity-like mode. For comparison, the attenuation levels obtained with the plate-based H^∞ /MinMax full state control law are also summarized in the tables.

As noted by the rms sound pressure levels in Table 7, the plate-based compensator is fairly effective in attenuating noise generated primarily by a plate-like mode. The results in Table 8 illustrate that this strategy is ineffective (at some points, sound pressure levels are actually increased) for exogenous frequencies driving cavity-like modes (this reinforces observations made in [13, 20]). While rms displacement levels are reduced by a factor of nearly four, sound pressure levels remain high due to the effective structural acoustic coupling. To attain an effective compensator for general frequencies, the coupling mechanisms and acoustic components *must* be incorporated in the model and control law.

	Pressure level (dB)			Displacement (m)
	c_1	c_2	c_3	p_1
open loop	116.4	105.4	112.4	5.254×10^{-4}
H^∞ full state	107.7	101.4	105.2	0.464×10^{-4}
H^∞ compensator	109.5	103.4	109.2	0.950×10^{-4}

Table 7. Sound pressure and displacement levels (rms) for the 65 Hz exogenous force $f_1(t)$.

	Pressure level (dB)			Displacement (m)
	c_1	c_2	c_3	p_1
open loop	122.5	117.4	122.9	0.413×10^{-4}
H^∞ full state	124.9	119.8	125.3	0.133×10^{-4}
H^∞ compensator	125.5	120.4	125.9	0.342×10^{-4}

Table 8. Sound pressure and displacement levels (rms) for the 165 Hz exogenous force $f_2(t)$.

7 Conclusion

The utilization of coupling effects in control design for structural acoustic systems was considered in this work. One objective in many such systems is the attenuation of structure-borne noise through the use of surface-mounted actuators such as piezoceramic patches. Models for such systems thus have a structural/actuator component, acoustic field components and coupling mechanisms which model the acoustic/structure interactions. It is through these coupling mechanisms that feedback control of noise through the structural actuators can be accomplished.

The prototypical experimental setup considered here consisted of a cylindrical acoustic cavity with a driven circular plate mounted at one end. Piezoceramic patch pairs driven out-of-phase to produce pure bending moments were used as actuators. A PDE system was used to model the structural, acoustic and coupling components for this setup. Galerkin approximations were used to obtain an ODE system suitable for simulation, parameter estimation and control applications.

For this modeled system with full coupling (backpressure and velocity) between the structure and adjacent acoustic field, numerical simulations demonstrated a 1-5 Hz shift in system frequencies from those observed for the isolated components. The backpressure from the field on the plate produced plate-like system frequencies lower than those of the isolated plate; hence through the coupling, the field acts as added mass to the plate. The coupling of the plate to the acoustic field produces an opposite stiffening effect in that system frequencies of acoustic-like modes are higher than isolated acoustic frequencies. For the geometry in these examples, the frequency shifts were fairly small and one might obtain reasonable modal information about the system through consideration of the uncoupled structure and acoustic field. In general, however, if coupling mechanisms are not included in the model, the frequency inaccuracies can nullify and possibly destabilize the controller.

The utilization of the coupling mechanisms can, on the other hand, lead to very effective controllers. To illustrate this, two sets of H^∞ /MinMax control laws were considered. Full state information was assumed for the first while the states were estimated from sensor measurements and then employed in an output feedback law in the second. In the latter (the MinMax compensator), a variety of sensor arrangements were compared to determine the extent to which the coupling could be utilized.

For various exogenous inputs, numerical simulations demonstrated high attenuation with both the full state feedback law and the output feedback law with states reconstructed using pressure, velocity and displacement measurements. More importantly, the results demon-

strated only a 1-2 dB loss of control when state measurements used for feedback were obtained *only* from structural velocity sensors. This latter case is important since it demonstrates that through the coupled structural acoustic model, accurate acoustic state information can be obtained *solely* from velocity measurements. This has important ramifications in a large number of structural acoustic systems since it demonstrates the possibility of eliminating pressure sensors (microphones) in the field (microphones in a fuselage can be unwieldy while microphones outside a submarine are unreasonable).

Finally, numerical results demonstrating the necessity of retaining the coupling and acoustic components when designing a general control law for noise attenuation were presented. These results demonstrate that while a control law based solely on the structural component can be effective for exogenous frequencies near plate-like frequencies, it is totally ineffective for applications in which cavity-like modes are excited. This reinforces the necessity of careful modeling of the structural, acoustic and coupling components and the design of a compensator which utilizes all three components.

Acknowledgements: The authors thank R.J. Silcox, Acoustics Division, NASA Langley Research Center, for numerous discussions related to practical control implementation in structural acoustic systems.

References

- [1] T. Başar and P. Bernhard, *H[∞]-Optimal Control and Related Minimax Design Problems*, Birkhäuser, Boston-Basel-Berlin, 1991.
- [2] H.T. Banks, M.A. Demetriou, and R.C. Smith, "An H^∞ Min/Max Periodic Control in a 2-D Structural Acoustic Model with Piezoceramic Actuators," *IEEE Transactions on Automatic Control*, 41(7), 1996, pp. 943-959.
- [3] H.T. Banks, M.A. Demetriou and R.C. Smith, "Robustness Studies for H^∞ Feedback Control in a Structural Acoustic Model with Periodic Excitation," *International Journal of Robust and Nonlinear Control*, 6, 1996, pp. 453-478.
- [4] H.T. Banks, M.A. Demetriou and R.C. Smith, "Utilization of Coupling Effects in Compensator Design for Structural Acoustic Systems – Numerical Results," CRSC Technical Report 96-24, August 1996.
- [5] H.T. Banks, W. Fang, R.J. Silcox, and R.C. Smith, "Approximation Methods for Control of Structural Acoustics Models with Piezoceramic Actuators," *Journal of Intelligent Material Systems and Structures*, 4, 1993, pp. 98-116.
- [6] H.T. Banks and R.C. Smith, "Parameter Estimation in a Structural Acoustic System with Fully Nonlinear Coupling Conditions," *Mathematical and Computer Modeling*, 23(4), 1996, pp. 17-50.

- [7] H.T. Banks and R.C. Smith, "The Modeling and Approximation of a Structural Acoustics Problem in a Hard-Walled Cylindrical Domain," CRSC Technical Report CRSC-TR94-26, December 1994; in *Dynamics and Control of Distributed Parameter Systems*, H.S. Tzou and L.A. Bergman, eds., Cambridge University Press, 1996, to appear.
- [8] H.T. Banks, R.C. Smith, D.E. Brown, V.L. Metcalf and R.J. Silcox, "The Estimation of Material and Patch Parameters in a PDE-Based Circular Plate Model," CRSC Technical Report CRSC-TR95-24, July 1995; *Journal of Sound and Vibration*, to appear.
- [9] H.T. Banks, R.C. Smith, D.E. Brown, R.J. Silcox, and V.L. Metcalf, "Experimental Confirmation of a PDE-Based Approach to Design of Feedback Controls," ICASE Report 95-42, May 1995; *SIAM J. Control and Optimization*, to appear.
- [10] H.T. Banks, R.C. Smith, and Y. Wang, *Smart Material Structures: Modeling, Estimation and Control*, Masson/John Wiley, Paris/Chichester, 1996.
- [11] H.T. Banks, R.C. Smith, and Y. Wang, "The Modeling of Piezoceramic Patch Interactions with Shells, Plates and Beams," *Quart. Appl. Math.*, 53(2), June 1995, pp. 353-381.
- [12] W.T. Baumann, W.R. Saunders and H.H. Robertshaw, "Active Suppression of Acoustic Radiation from Impulsively Excited Structures," *J. Acoust. Soc. Am.*, 90(6), 1991, pp. 3202-3208.
- [13] R.L. Clark and C.R. Fuller, "A Model Reference Approach for Implementing Active Structural Acoustic Control," *J. Acoust. Soc. Am.*, 92(3), 1992, pp. 1534-1544.
- [14] C.E. deSouza, U. Shaked, and M. Fu, "Robust H_∞ Tracking: A Game Theory Approach," *International Journal of Robust and Nonlinear Control*, 5 (1995), pp. 223-238.
- [15] A. Frendi, L. Maestrello and A. Bayliss, "Coupling between Plate Vibration and Acoustic Radiation," *Journal of Sound and Vibration*, 177(2), 1994, pp. 207-226.
- [16] A. Frendi, L. Maestrello, J. Robinson and A. Bayliss, "On Acoustic Radiation from a Vibrating Panel," Proceedings of the 15th AIAA Aeroacoustics Conference, Long Beach, CA, October 25-27, 1993.
- [17] A. Frendi and J. Robinson, "Effect of Acoustic Coupling on Random and Harmonic Plate Vibrations," *AIAA Journal*, 31(11), 1993, pp. 1992-1997.
- [18] C.R. Fuller, C.A. Rogers and H.H. Robertshaw, "Active Structural Acoustic Control with Smart Structures," Proceedings of the SPIE Conference 1170 on Fiber Optic Smart Structures and Skins II, Boston, MA August 5-8, 1989.
- [19] B.V. Keulen, *H_∞ -Control for Distributed Parameter Systems: A State-Space Approach*, Birkhäuser, Boston-Basel-Berlin, 1993.
- [20] J. Pan and C.H. Hansen, "Active Control of Noise Transmission through a Panel into a Cavity. II: Experimental Study," *J. Acoust. Soc. Am.*, 90(3), 1991, pp. 1488-1492.

- [21] C.R. Fuller, S.D. Snyder, C.H. Hansen and R.J. Silcox, Active control of interior noise in model aircraft fuselages using piezoceramic actuators, Paper 90-3922, AIAA 13th Aeroacoustics Conference, Tallahassee, FL, October 1990.
- [22] R.C. Smith, "A Galerkin Method for Linear PDE Systems in Circular Geometries with Structural Acoustic Applications," ICASE Report 94-40, 1995, *SIAM Journal of Scientific Computing*, to appear.
- [23] A. Stoorvogel, *The H^∞ Control Problem*, Prentice Hall, Englewood Cliffs, NJ, 1992.